AUTHOR(S):

Yokoyama, Y.; Taguchi, S.; Iyemori, T.; Hosokawa, K.

JGR Space Physics

RESEARCH ARTICLE

Key Points:
- Irregular magnetic perturbations occur in the dusk part of the auroral oval instead of Region 1/2 magnetic perturbations
- The irregular magnetic perturbations are a result of highly structured quasistatic field-aligned currents
- The highly structured field-aligned currents are the phenomena pertinent to the magnetosphere for a northward IMF condition

Correspondence to:
Y. Yokoyama,
yokoyama@kugi.kyoto-u.ac.jp

The Quasipersistent Feature of Highly Structured Field-Aligned Currents in the Duskside Auroral Oval: Conjugate Observation Via Swarm Satellites and a Ground All-Sky Imager

Y. Yokoyama[1] [ID], **S. Taguchi[1,2]** [ID], **T. Iyemori[2]** [ID], **and K. Hosokawa[3,4]** [ID]

[1]Department of Geophysics, Graduate School of Science, Kyoto University, Kyoto, Japan, [2]Data Analysis Center for Geomagnetism and Space Magnetism, Graduate School of Science, Kyoto University, Kyoto, Japan, [3]Department of Communication Engineering and Informatics, University of Electro-Communications, Tokyo, Japan, [4]Center for Space Science and Radio Engineering, University of Electro-Communications, Tokyo, Japan

Abstract During northward interplanetary magnetic field (IMF), irregular magnetic perturbations were observed in the duskside aurora oval via Swarm satellites instead of large-scale Region 1/2 magnetic perturbations. By taking advantage of Swarm constellation measurements, and their conjugate observations with an all-sky imager on the ground, the features of the irregular magnetic perturbations were examined. Detailed analysis of the data from Swarm A and Swarm C for two events demonstrated that the irregular magnetic perturbations are a result of highly structured quasistatic field-aligned currents (FACs), not dynamic Alfvén waves. The typical latitudinal size of the upward FACs is 20–30 km. In each region of the upward FACs, 630-nm aurora emissions are relatively strong, indicating that the energy flux of precipitating electrons having energies of a few hundred electron volts is high in each of the upward FAC regions. The enhanced mesoscale auroras continued to exist for at least approximately 30 min. These indicate that the mesoscale FAC structures also have quasipersistent features. The precipitating particle data from the Defense Meteorological Satellite Program satellite, which passed through the field of view of the all-sky imager, indicate that the source of the precipitating particles is the duskside low-latitude boundary layer (LLBL). We suggest that the highly structured quasipersistent FACs flow along the magnetic field lines connected to the duskside LLBL where cold dense ions exist. The highly structured FACs in the duskside aurora oval are the phenomena that are pertinent to the magnetosphere for a northward IMF condition, not a simple remnant of the typical Region 1.

1. Introduction

The Region 1 field-aligned current (FAC), which flows into or away from the high-latitude part of the auroral oval in the ionosphere, generally increases its current intensity irrespective of magnetic local time (MLT) as the southward component of interplanetary magnetic field (IMF) increases (e.g., Weimer, 2001; Papitashvili & Rich, 2002). When the IMF has a strong northward component, that is, during a prolonged geomagnetic quiet time, Region 1 nearly diminishes except its near-noon part, and small-amplitude irregular magnetic perturbations occur at latitudes where Region 1 FAC disappeared (Rich & Gussenhoven, 1987). Whether these small-amplitude irregular magnetic perturbations simply reflect a "remnant" of Region 1 FAC or represent phenomena independent of Region 1 FAC, which can become prominent particularly during a strong northward IMF, has not been understood yet.

To understand the features of these irregular magnetic perturbations observed by low-altitude spacecraft, it is important to know to what extent these magnetic perturbations are produced by the quasistatic structure of the FACs; in other words, to what extent these magnetic perturbations include a temporal variation of the Alfvén waves. At an altitude range of from ~5,000 to 10,000 km, which is much higher than the ionospheric altitude, magnetic and electric field fluctuations associated with Alfvén waves are clearly observed by spacecraft (e.g., Matsuoka et al., 1993; Weimer et al., 1985). At altitudes below ~1,000 km, the Alfvénic variations tend to be observed at horizontal scale sizes that are shorter than 32–64 km along the satellite pass of the low-altitude spacecraft (Ishii et al., 1992). At these horizontal scales, polarization features suggesting the existence of Alfvén waves or ion cyclotron waves are also observed (Ishii et al., 1992; Iyemori,

1988). A recent study that used magnetic field measurements sampled at 50 Hz from Swarm A (SW-A) and Swarm C (SW-C), whose altitudes are ~450 km, shows an example in which ~100-nT amplitude magnetic variations observed on the dawnside have Alfvénic features (Pakhotin et al., 2018). Notably, however, these studies, which are based on low-altitude satellites, do not claim that magnetic perturbations whose horizontal scale sizes are shorter than several tens of kilometers along the satellite pass are totally produced by the dynamic Alfvén waves.

Multisatellite observations at the same position but at two different times are of great help in understanding to what extent magnetic perturbations are produced by a dynamic Alfvén wave or the quasistatic structure of FACs. Gjerloev et al. (2011) presented comprehensive statistical study of the spatiotemporal characteristics of FACs using multipoint measurements by three ST-5 satellites. They concluded that the characteristics of large-scale FAC system, whose scale sizes are larger than ~200 km at ionosphere altitudes, appear to be quasistatic. Lühr et al. (2015) also examined the temporal and spatial scales of FAC structures derived from Swarm constellation measurements. They showed that a large-scale FAC, defined as that greater than 150 km, can be regarded as being quasistatic, while small-scale FACs up to approximately 10 km, are highly variable in amplitude, which can be ascribed to the Alfvén waves, and a persistent period of the small-scale FACs is on the order of 10 s or less.

The purpose of this paper is to clarify the features of the irregular magnetic perturbations that are seen at latitudes where Region 1 FAC disappears by taking advantage of Swarm constellation measurements and their conjugate observations with a ground-based all-sky imager. We focus on the duskside MLT where Region 1 flows away from the ionosphere. The disappearance of upward Region 1 might considerably weaken the concurrent electron precipitation, making the auroral emission obscure. Otherwise, the electron precipitation may show some small-scale structures or some temporal features consistent with the spatial structure of FACs or with the period of the Alfvén wave, respectively.

2. Data

Swarm consists of three identical near-polar orbiting satellites, A, B, and C. Each of the three satellites carries the fluxgate magnetometer and measures the magnetic field vector (Friis-Christensen et al., 2006). In this study, we subtracted the International Geomagnetic Reference Field (IGRF-12, Thébault et al., 2015) from the coordinate converted magnetic field vector in the North-East-Center local Cartesian (NEC) coordinates, whose resolution is 1 Hz, and analyzed the magnetic perturbation data.

Among the three satellites, SW-A and SW-C have been flying side by side, separated by 1.4° in longitude at approximately 460 km altitude with a slight time difference since April 2014. The magnetic perturbation data obtained by the two satellites are useful to understand whether or not FACs, which cause the magnetic perturbations, are stable during such a short time period. SW-A and SW-C were approximately 10 s apart along the track.

The all-sky imager that we used is in Longyearbyen, Norway (Taguchi et al., 2012). This imager has been operative since October 2011. The imager is equipped with an electron multiplier charge-coupled device camera (Hamamatsu, C9100-13) with an imaging resolution of 512×512 pixels and measures emissions at two wavelengths, 557.7 and 630.0 nm. The 630-nm image data can provide detailed information regarding electron precipitation having energies of a few hundred electron volts (e.g., Roble & Rees, 1977). We used 630-nm all-sky image data obtained with an exposure time of 1 s. Data obtained with an exposure time of 4 s are also available (Taguchi et al., 2015), but those are usually suitable for identifying the structure of faint emissions from the polar cap patches (e.g., Hosokawa et al., 2013).

We analyzed the data obtained during the period November 2014 to January 2015, which is the first winter season after SW-A and SW-C taking the aforementioned configuration. The all-sky image was converted into the altitude adjusted corrected geomagnetic (AACGM) coordinates (Baker & Wing, 1989) under the assumption that the 630-nm emission height is 250 km and mapped into coordinates of magnetic latitude (MLAT) and MLT.

From the aforementioned 3-month period, we searched for intervals during which SW-A and SW-C transected the field of view of the all-sky imager on the duskside (defined as 14–18 MLT), and the IMF had a positive Z component in the geocentric solar magnetospheric (GSM) coordinate system continuously for at least

for 40 min before the time when SW-C crossed 80° MLAT. At earlier MLT sector (say <14 MLT) cusp, FACs tend to be observed (e.g., Taguchi et al., 1993; Wing et al., 2010), and we excluded these MLT regions. For IMF, we used OMNI 5-min data. Two events were found in which the clear all-sky image data are available, and the horizontal magnetic perturbations observed by both satellites are so structured that large-scale Region 1/2 current system cannot be unambiguously determined.

3. Results

3.1. Overview of the 17 January 2015 Event

Figure 1a shows one of the two events, which occurred on 17 January 2015. The magnetic perturbations (east-west component) observed by SW-C on the duskside during the period 12:57:30–13:01:30 UT are plotted. The magnetic perturbations are highly structured at ~75° to ~80° MLAT. The positive and negative gradients of the magnetic perturbations indicate FACs flowing away from and into the ionosphere, respectively. Multiple mesoscale FACs can be observed. We hereinafter use the term mesoscale as a spatial scale ranging from ~10 to 100 km as in Hasunuma et al. (2008).

Figure 1b shows the magnetic perturbations from the next SW-C pass. In this pass, SW-C traversed a similar region on the MLT-MLAT dial. A large-scale upward Region 1 FAC and downward Region 2 FAC are clearly seen. When the magnetic perturbations shown in Figure 1a are compared with those shown in Figure 1b, it is evident that large-scale Region 1 and Region 2 FACs are absent during the first pass.

Figure 1c shows one of the auroral images obtained during the interval when SW-C passed through the field of view of the auroral imager. The footprint of the satellite's trajectory is shown by the white line. SW-C passed through the auroras between ~77° and ~80° MLAT. Relations between the SW-C magnetic perturbations and these aurora structures are examined later. Emissions at much lower latitudes, which are seen near the sunward boundary of the field of view, are simply the sunlight beneath the horizon and not auroras.

Figure 2 shows the solar wind and IMF data from OMNI and the SYM-H index between 12:00 UT and 15:00 UT on 17 January 2015. From top to bottom, the three components of IMF (B_X, B_Y, and B_Z) in the GSM coordinates, IMF clock angle, defined as $\tan^{-1}(B_Y/B_Z)$; cone angle, defined as $\cos^{-1}(B_X/B_T)$; solar wind proton density; flow speed; dynamic pressure; and the SYM-H index are plotted. B_T is the total magnitude of the IMF. Two vertical dotted lines at 12:58:16 UT (left) and 14:32:48 UT (right) indicate the times for the data shown in Figure 1a (i.e., the 17 January 2015 event) and Figure 1b (the Region 1/2 event), respectively. We use here the time when SW-C crossed 80° MLAT in the dusk region. We did not take into account the time lag between the time shown in the OMNI solar wind data and the actual measurement at ionospheric altitudes.

The B_Z was approximately constant at ~2.9 nT for 40 min before the time shown by the left dotted line. At approximately the time shown by the right dotted line, IMF also took a positive B_Z; however, there was an interval of negative B_Z (from 14:00:00 to 14:15:00 UT) shortly before this time. B_Y was approximately constant throughout the plotted interval, and the average over 40 min before the 17 January 2015 event (left dotted line) was ~3.7 nT. The clock angle for that interval was between 44° and 86°. B_X was approximately constant at approximately −2.1 nT during this time period. The cone angle was predominantly between 67° and 77°. The solar wind proton density, speed, and dynamic pressure were very stable for 40 min before the event; the averages of the solar wind density, speed, and dynamic pressure over the 40 min are 5.0 cm^{-3}, 350 km s^{-1}, and 1.2 nPa, respectively. The OMNI solar wind plasma data at 13:00:00 UT are not available; however, the flat variations seen in the SYM-H index show that there were no particular enhancements in the solar wind dynamic pressure at that time.

3.2. Multiple FACs and Auroras During the 17 January 2015 Event

Figure 3a shows the east-west magnetic perturbations observed by SW-A from 12:57:00 to 13:01:30 UT on 17 January 2015. These magnetic perturbations are highly structured as shown in the data obtained during the same interval by SW-C (Figure 1a). The expanded plots of the data for the period 12:58:20–12:59:20 UT are shown in Figure 3b (for SW-A) and Figure 3d (for SW-C). Figures 3c and 3e show the FAC densities derived from the magnetic perturbations obtained by SW-A and SW-C under the assumption of an infinite current sheet, which is perpendicular to the satellite orbit, respectively. Note that the vertical axis of these plots is inverted such that the negative current density, which is antiparallel to the Earth magnetic field in the
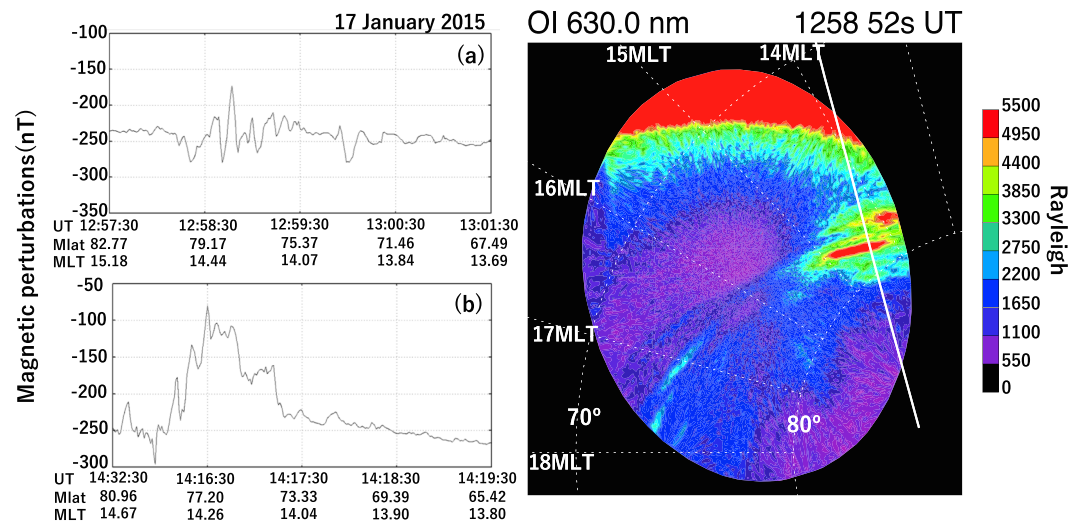
Figure 1. The magnetic perturbations (east-west component) observed by SW-C on the duskside (a) during 12:57:30–13:01:30 UT on 17 January 2015 and (b) during 14:32:30–14:16:30 UT from next SW-C pass. (c) One of the auroral images obtained during the interval when SW-C passed through the field of view of the auroral imager. The footprint of the satellite's trajectory is shown with the white line.

northern ionosphere, can be shown in an upward direction. Multiple upward/downward FACs can be seen in both the data. The red vertical lines in Figures 3b and 3c represent the three (not all) crossing times of the upward FAC region. These times, that is, 12:58:31, 12:58:50, and 12:58:59 UT, are used for comparison with the auroral data later. When the variations seen in Figure 3c (or Figure 3b) are compared with those in Figure 3e (or Figure 3d), it is evident that similar variations occur within the time lag of approximately 10 s.

Figure 3f shows how highly these variations are correlated. The vertical axis of Figure 3f represents how much time we advanced the SW-A data for the purpose of calculating the correlation coefficient. For example, the correlation coefficient at 10 s originates from the SW-C data and 10-s advanced SW-A data. We used 30 data points (=30 s) around a given time and moved the data window by 1 s. The correlation coefficients are very high (yellow color in Figure 3f) for the advance time of 9 s throughout the plotted interval. In Figure 3g, the 9-s shifted SW-A data (red solid line) are superposed on the SW-C data (blue solid line). These data overlap very well, as expected. It is obvious from Figures 3f and 3g that the observed magnetic perturbations represent the spatial structure of the quasistatic FACs.

Figures 3h–3j show the 630-nm auroral images, each of which was obtained at the time nearest to the crossing time of the upward FAC region (the three vertical red lines in Figures 3b and 3c). The small black and white solid circles in each image indicate the footprints of SW-A and SW-C, respectively. As shown by three arrows in Figure 3h, each image shows that there are three regions of relatively strong auroral emissions between 76° MLAT and 80° MLAT. At 12:58:25 UT, the footprint of SW-A was immediately poleward of one of the three auroral structures (Figure 3h). Then, the footprint passed through the auroral structure and was in the middle auroral structure at 12:58:52 UT (Figure 3i). At 12:58:57 UT, the footprint was in the lowest-latitude auroral structure (Figure 3j). These show that strong auroral emissions occur in each of the upward FAC regions. In other words, how long the distribution of the upward FACs continues can be inferred from the stability of the auroral structures, as discussed later.

3.3. 22 December 2014 Event

Figure 4 shows the solar wind and IMF data from OMNI and the SYM-H index for the second event, that is, the 22 December 2014 event. From top to bottom, the three components of IMF (B_X, B_Y, and B_Z) in the GSM coordinate, IMF clock angle, cone angle, solar wind proton density, flow speed, dynamic pressure, and SYM-H index are plotted.

Both B_Z and the B_Y were large positive and approximately constant for more than 1 hr before the event (the dotted line shown in Figure 4). The average B_Z and B_Y over 40 min before the event are ~10.0 and ~12.5 nT,
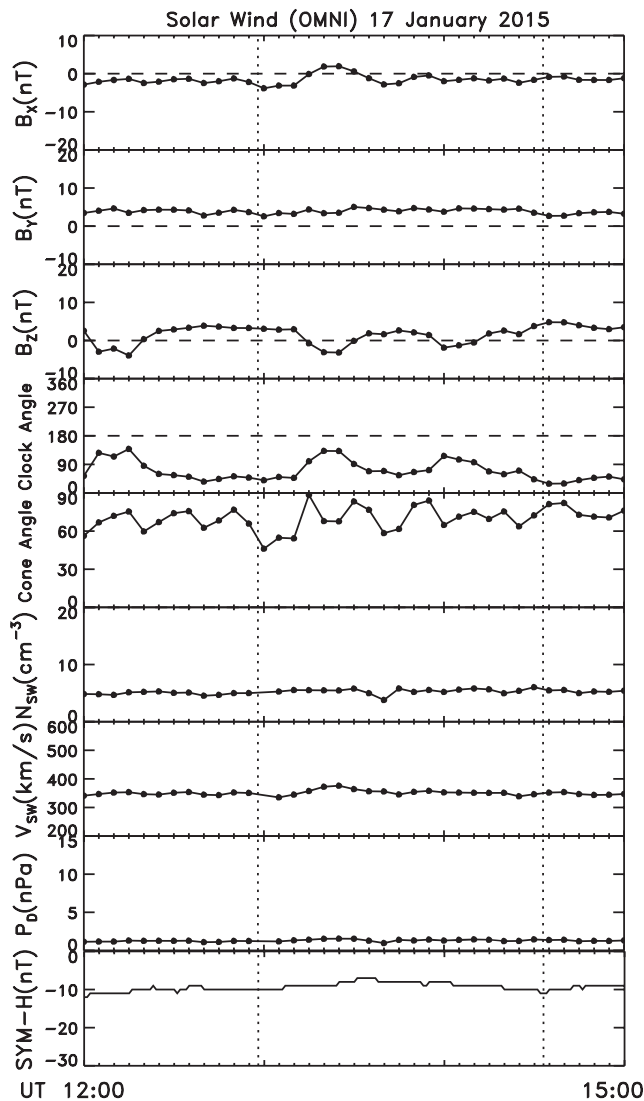
Figure 2. The solar wind and IMF data from OMNI and the SYM-H index between 12:00 UT and 15:00 UT on 17 January 2015. From top to bottom, the three components of IMF (B_X, B_Y, and B_Z) in GSM coordinate, the IMF clock angle, defined as $\tan^{-1}(B_Y/B_Z)$, the cone angle, defined as $\cos^{-1}(B_X/B_T)$, the solar wind proton density, the flow speed, the dynamic pressure, and the SYM-H index are plotted. B_T is the total magnitude of IMF. Two vertical dotted lines at 12:58:16 UT (left) and 14:32:48 UT (right) indicate the times for the data shown in Figures 1a and 1b, respectively.

respectively. The clock angle for this interval was between 47° and 53°. B_X was approximately constant at approximately -5.6 nT during this period of time. The cone angle was predominantly between 66° and 74°. The solar wind proton density, speed, and dynamic pressure were very stable over 40 min before the event; the averages of the solar wind proton density, speed, and dynamic pressure are approximately 6.8 cm^{-3}, 370 km s^{-1}, and 1.9 nPa, respectively. Notably, a sudden commencement occurred at ~15:11 UT responding to the increase in the dynamic pressure.

Figure 5 shows the data from SW-A, SW-C, and the auroral imager in the same format as Figure 3 except for the number of the auroral images. Figure 5a shows the east-west magnetic perturbations that were observed by SW-A during the period 14:41:40–14:46:20 UT. The magnetic perturbations are highly structured similar to those for the 17 January 2015 event. Figures 5b–5e are the plots of the data for the period 14:43:20–14:44:40 UT. Multiple upward/downward FAC regions exist. The red vertical lines shown in Figures 5b and 5c represent the crossing times of the four well-defined upward FACs.

Figure 5f shows the result of cross-correlation analysis between SW-A and SW-C data. It is obvious that the correlation coefficients are very high for the 9-s advanced SW-A and SW-C (yellow color in Figure 5f). As can be seen in Figure 5g, the 9-s shifted SW-A data and SW-C data overlap very well. Undoubtedly, the observed magnetic perturbations represent the spatial structure of the quasistatic FACs.

Figures 5h–5k show the 630-nm auroral images, each of which was obtained at the time nearest to the crossing time of the upward FAC region (the four vertical red lines in Figures 5b and 5c). As is shown by the four arrows in Figure 5h, there were four regions of relatively strong auroral emissions between 76° and 80° MLAT at 14:43:37 UT. At this time, the footprint of SW-A was in one of the four auroral structures. Thereafter, the footprint passed through that auroral structure and was in the vicinity of the second auroral structure at 14:43:51 UT (Figure 5i). At 14:44:10 UT, the footprint was in the third auroral structure (Figure 5j). At 14:44:23 UT, the footprint was near the fourth auroral structure, although the boundary of the aurora was not very clear at this time (Figure 5k). In a similar manner to that of the 17 January 2015 event, relatively strong auroral emissions occurred in the upward FAC regions.

Immediately before the beginning of the plotted interval of Figure 5a, DMSP F16 spacecraft passed through the imager's field of view. Figure 6a shows the trajectory of DMSP F16 between 14:37:00 and 14:39:00 UT, mapped on the 630-nm auroral image obtained at 14:38:01 UT. The two arrows in the image indicate the regions of relatively strong auroral emissions.

Figure 6b shows the data from the DMSP F16 magnetic field experiments and particle spectrometer from 14:35:00 to 14:40:00 UT. The top panel shows the Z component of the baseline-corrected magnetic field perturbation data in the spacecraft coordinates. Two sharp negative gradients (from 14:37:33 to 14:37:40 UT and from 14:38:12 to 14:38:27 UT) occur as indicated by the four dotted lines in the top panel. These gradients represent upward FACs. At the bottom, the energy fluxes of the electrons and ions are plotted with color codes, together with the integral energy flux and average energy of the electrons and ions. Note that the ion energy axis is inverted in the fourth panel.
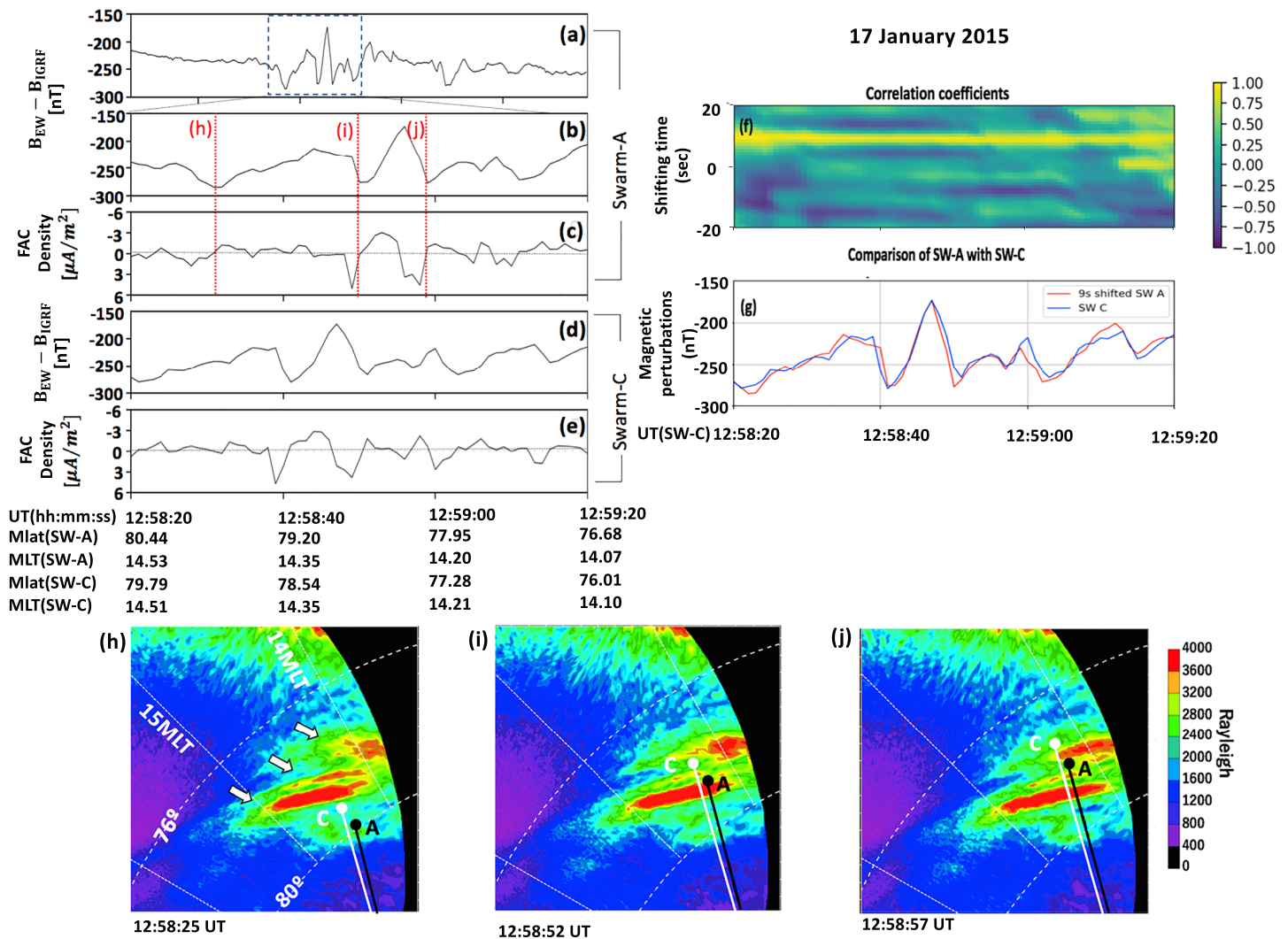
Figure 3. Multiple field-aligned currents and auroras in 17 January 2015 event. (a) The east-west magnetic perturbations observed by Swarm A (SW-A) from 12:57:00 to 13:01:30 UT. (b, d) The expanded plots of the magnetic perturbations for 12:58:20–12:59:20 UT for SW-A and Swarm C (SW-C), respectively. (c, e) The FAC densities that are derived from the magnetic perturbations obtained by SW-A and SW-C under the assumption of infinite current sheet, which is perpendicular to the satellite orbit. The vertical axis of plots is inverted so that the negative current density can be shown in an upward direction. The red vertical lines in (b) and (c) represent the three crossing times of the upward FAC region. (f) The correlation coefficient of SW-A and SW-C magnetic data. The vertical axis represents how much time we advanced the SW-A data (see section 3.2). (g) The comparison plot that superposed the 9-s shifted SW-A data (red solid line) on the SW-C data (blue solid line). (h–j) The 630-nm auroral images, each of which was obtained at the time nearest to the crossing time of the upward FAC region (three vertical red lines in Figures 3b and 3c). The black and white solid circles in each image indicate the footprints of SW-A and SW-C, respectively. As is shown by three arrows in Figure 3h, each image shows that there are three regions of relatively strong aurora emissions between 76 MLAT and 80 MLAT.

DMSP F16 entered the region of low-energy (less than a few hundred electron volts) electron precipitation at 14:37:10 UT (the left dotted line in the bottom two panels). Precipitating ions with relatively low energy (down to a few hundred electron volts) also became evident following this entry, suggesting that cold dense ions occur in the source region of FACs (e.g., Fujimoto et al., 1998; Terasawa et al., 1997). The source region appears to be the low-latitude boundary layer (LLBL). The right dotted line indicates the poleward boundary of that region, that is, 14:38:27 UT. At the next time (14:38:28 UT), the electron energy fluxes at the energy bins between ~200 and ~450 eV decreased to values less than 1×10^8 eV cm^{-2} s^{-1} sr^{-1} eV^{-1}. The poleward boundary (14:38:27 UT) corresponds to the poleward edge of one of the upward FACs previously noted. Poleward of this boundary, a brief gap of electron precipitation occurred. At higher latitudes than this gap, a region of accelerated electron precipitation showing an inverted-V structure occurred. The aurora produced by this electron precipitation is also shown in Figure 6a. This auroral structure is at higher
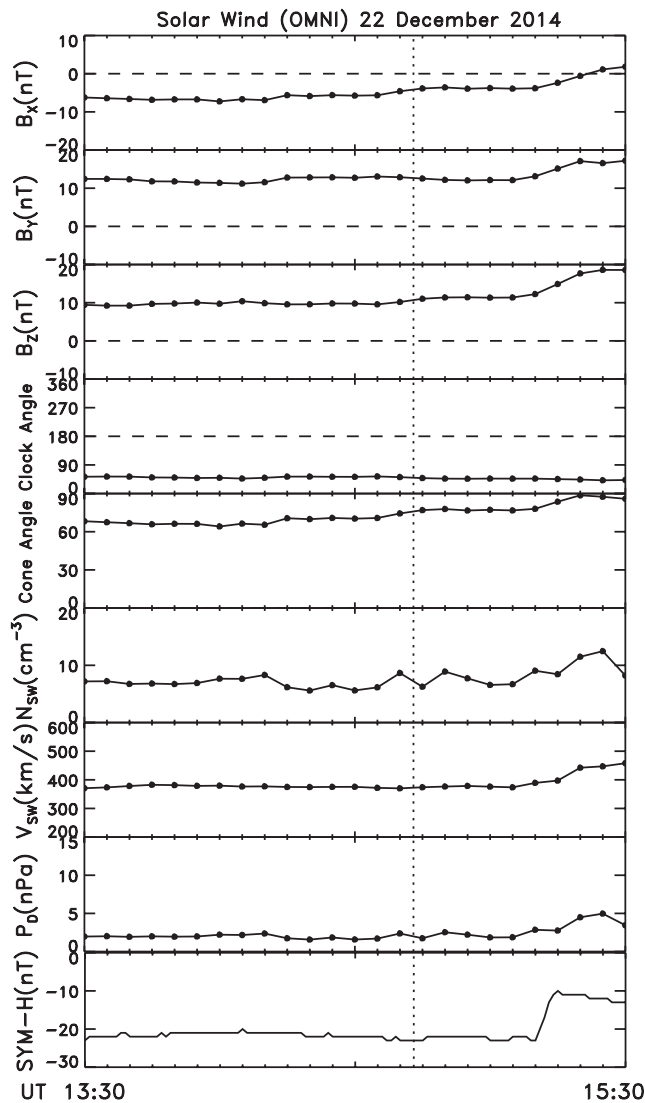
Figure 4. The solar wind and IMF data from OMNI and the SYM-H index between 13:30 UT and 15:30 UT on 22 December 2014 in the same format as Figure 2. The vertical dotted line indicates 14:43 UT when SW-C first entered the upward FAC regions.

latitudes than 80° MLAT. This appears to be the polar cap arc, which is often seen in the duskside polar cap when IMF B_Y is positive (e.g., Elphinstone et al., 1990; Gussenhoven, 1982).

The electron precipitation data also show that the LLBL region has a brief gap (14:38:06–14:38:12 UT) where the energy flux of the precipitating electrons at a few hundred electron volts was less than 1×10^8 eV cm^{-2} s^{-1} sr^{-1} eV^{-1}. This indicates that the electron precipitation forms a double structure, consistent with the fact that the auroral emissions were relatively strong at two latitudes (the two arrows in Figure 6a). Notably, this electron precipitation gap corresponds to the sharp positive gradient of the magnetic perturbations (top panel), that is, the region of downward FACs whose current density is relatively strong.

When the auroral image shown in Figure 6a is compared with the images shown in Figures 5h–5k, two auroral structures, seen at 14:38:01 UT (Figure 6a), continued to exist until 14:44:23 UT (Figure 5k). Although observations of the precipitating electrons for the aurora seen between 14:43:37 and 14:44:23 UT (Figures 5h–5k) are lacking, the persistent feature of the aurora, which continued from the time of the DMSP precipitating electron observations to 14:44:23 UT, suggests that the mesoscale FACs observed by SW-A or SW-C also flow along the magnetic field line connecting to the LLBL.

3.4. Latitudinal Size of the Mesoscale FAC

Figures 3g and 5g show that the magnetic perturbation data, whose resolution is 1 Hz, represent the spatial structure of quasistatic FACs. Figure 7 shows the distribution of the latitudinal size of the upward FAC observed by SW-A and SW-C from the two events. To calculate the latitudinal size, we multiplied the period of each upward FAC region by the satellites' velocity (7.8 km s^{-1}) and cos α, where α is an acute angle between the direction of the satellite orbit at the satellite's entry of each upward FAC region and the MLT meridian. We ruled out the very small-scale upward FAC (i.e., the calculated length of $\leq$7.8 km s^{-1}) embedded in a downward FAC region and required that the peak density of the upward FAC should be greater than 1 μA m^{-2}. From the histogram shown in Figure 7, it is evident that the typical size of the upward FAC region is 20–30 km.

3.5. Duration of the Mesoscale Aurora

Using the auroral images obtained before and after Swarm traversed the field of view of the all-sky imager, we examined how long similar mesoscale auroral structures continued to exist. Figure 8 shows six aurora images for the 17 January 2015 event and the temporal variation in the maximum intensity for three auroral structures together with the OMNI IMF data. The 2-hr (12:00 to 14:00 UT) OMNI IMF B_X, B_Y, and B_Z are plotted in Figure 8a. The vertical lines b–g in Figure 8a represent the time when each aurora image, shown on the right, was obtained.

Figure 8b is the image obtained at 12:52:14 UT. This image is the first 1-s exposure 630-nm image available for the dusk sector on this day. On this day, the imager was off between ~09:34 and ~12:52 UT. Two regions of relatively strong auroral emissions are seen in this image as shown with the white arrows (Aurora 1 and Aurora 2 in Figure 8b). In the image at 12:56:58 UT (Figure 8c), another region of enhanced emissions can be seen (Aurora 3). Aurora 3 became clear at 12:58:52 UT, while Aurora 2 was almost diminished at this time. Notably, the image shown in Figure 8d is the same as that in Figure 3i. Aurora 1 and Aurora 3 were still clear at 13:04:41 UT (Figure 8e). At the image obtained approximately 18 min later (Figure 8f), they were also
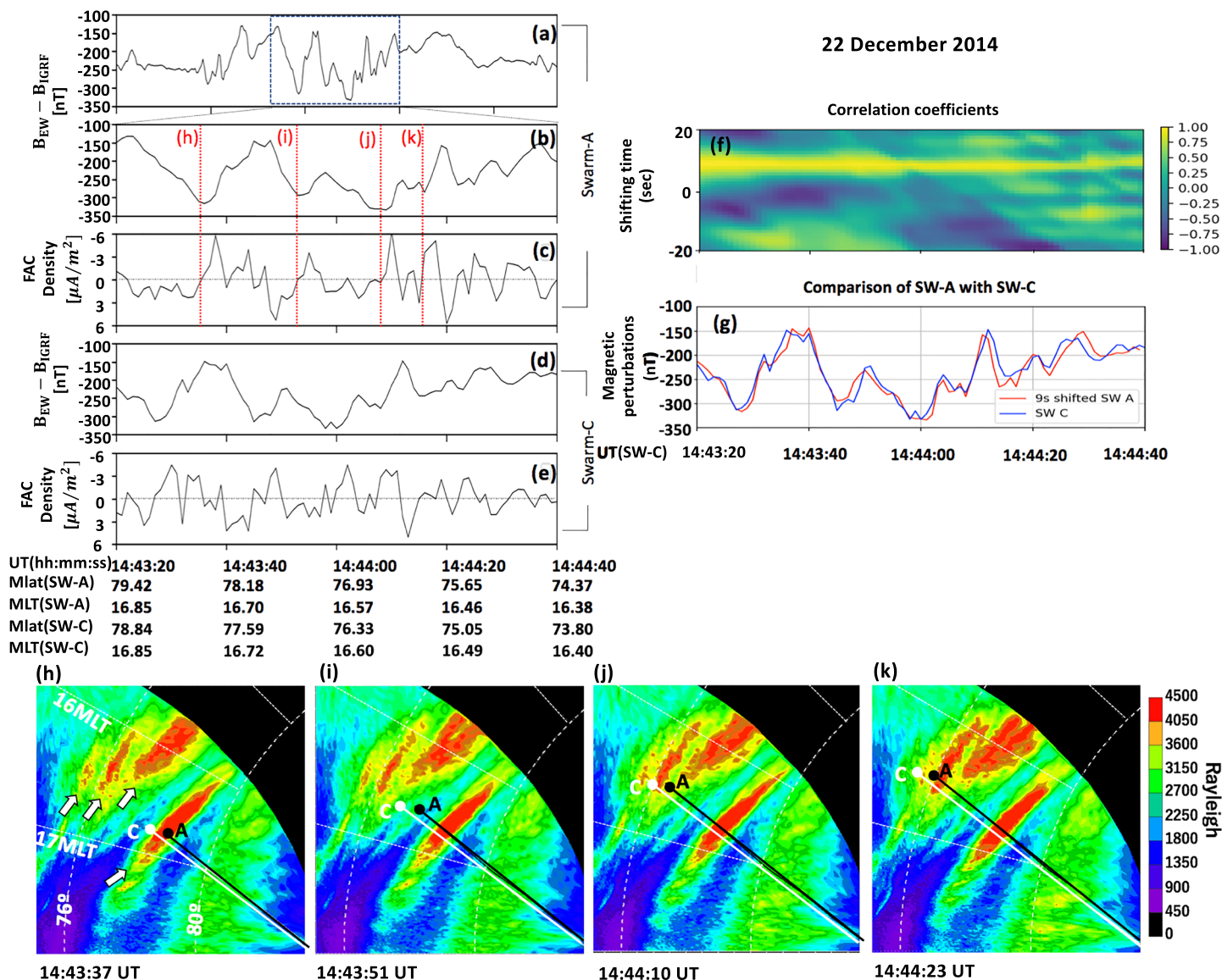
京都大学
KYOTO UNIVERSITY

Journal of Geophysical Research: Space Physics

10.1029/2019JA027594

京都大学学術情報リポジトリ
KURENAI 紅
Kyoto University Research Information Repository

Figure 5. Multiple field-aligned currents and auroras in 22 December 2014 event in the same format as Figure 3 except for the number of the aurora images. As is shown by four arrows in (h), there were four regions of relatively strong aurora emissions between 76 MLAT and 80 MLAT.

clearly seen, but the maximum intensity of Aurora 1 was rather weak. Finally, Aurora 1 became unclear (Figure 8g).

The temporal variations in the maximum intensities for Auroras 1, 2, and 3 are shown in Figure 8h. Note that the UT range of Figure 8h is not the same as that of Figure 8a. The aforementioned variation for Aurora 1 can be identified in Figure 8h. When we define the end time for Aurora 1 as the time when the maximum intensity inside Aurora 1 decreased to a value of <3,500 R (dotted line in Figure 8h), the duration of Aurora 1 can be estimated to be at least 30 min (~13:22:57 UT minus 12:54:14 UT). When applying the same definition to Aurora 3, it can be also estimated to be at least 30 min. The most enhanced emissions, that is, from ~13:00 to ~13:05 UT for Aurora 1 and from ~13:08 to ~13:15 UT for Aurora 3, occurred during the period of positive IMF B_Z, suggesting that the electron precipitation responsible for these auroral structures is related to the magnetospheric condition peculiar to a positive IMF B_Z.

Figure 9 shows six auroral images for the 22 December 2014 event and the temporal variation in the maximum intensity for three auroral structures together with the OMNI IMF data. The 2.5-hr (from 13:30 to 16:00 UT)
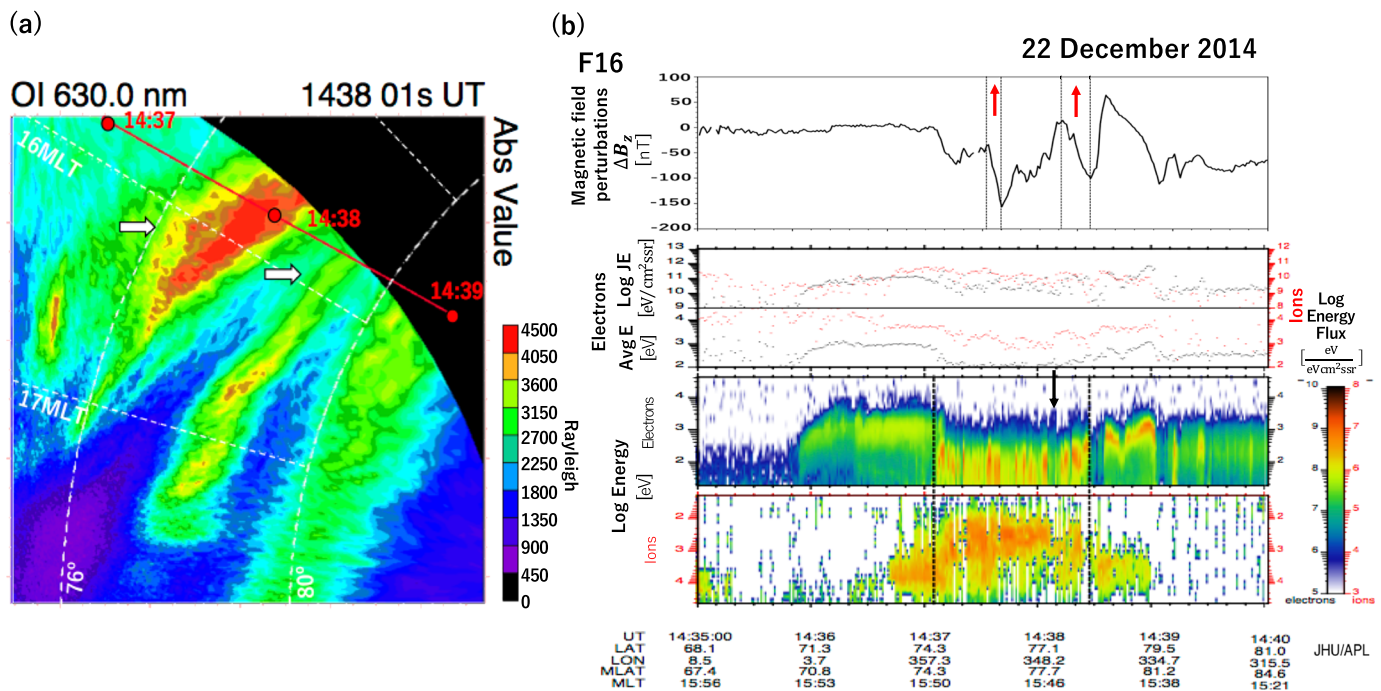
Figure 6. The DMSP F16 magnetic field experiments and particle spectrometer from 14:35:00 to 14:40:00 UT. (a) The trajectory of DMSF F16 between 14:37:00 and 14:39:00 UT, mapped on the 630-nm aurora image obtained at 14:38:01 UT. Two arrows in the image indicate the regions of relatively strong aurora emissions, which the footprint of the DMSP F16 trajectory may traverse. (b) The top panel shows Z component of the baseline-corrected magnetic field perturbation data in the spacecraft coordinates. There exist two sharp eastward gradient regions from 14:37:33 to 14:37:40 UT and from 14:38:12 to 14:38:27 UT, indicated by four dotted lines. In the bottom four panels, the energy fluxes of the electrons and ions are plotted with color codes, together with the integral energy flux and average energy of the electrons and ions. Note that ion energy axis is inverted in the fourth panel.

OMNI IMF B_X, B_Y, and B_Z are plotted in Figure 9a. The vertical lines b–g in Figure 9a represent the time when each auroral image, shown on the right, was obtained. Figures 9b and 9c show the auroral images obtained at 14:07:19 and 14:08:18 UT, respectively. From a comparison between these images, it is evident that a small-scale auroral structure, shown as Aurora 1 in Figure 8c, started to separate from the main aurora, shown as the "Equatorward Aurora" in Figure 8b, and intensified. We chose 14:08:18 UT as the time when the maximum intensity of Aurora 1 exceeded 2,500 R. Evidently, if we use a different threshold for the determination of the start time, the start time will change. However, as is shown in the following, the choice of this threshold will not affect our conclusion.
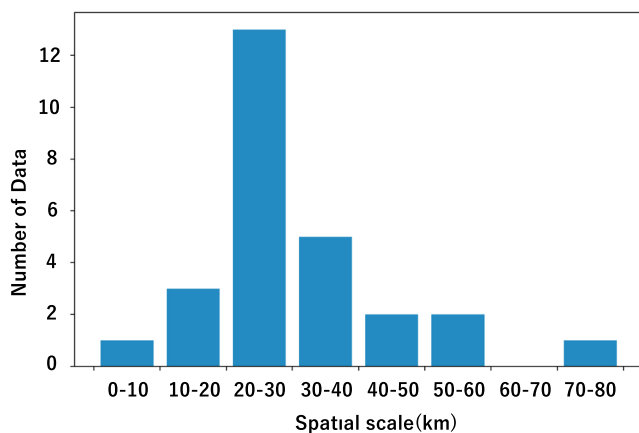
Aurora 1 then further intensified while moving slowly poleward. The image obtained approximately 30 min later (14:38:01 UT) has already been shown in Figure 6a, and the intensified features of Aurora 1 are clearly seen (right white arrow in Figure 6a). The image obtained at 14:43:37 UT is shown in Figure 9d. This image is the same as that shown in Figure 5h. Aurora 1 was still well separated from the other auroral emission regions. Figure 9e shows the image obtained at 15:08:04 UT. Aurora 1 was still clear at this time. Aurora 1 can be clearly seen until ~15:30 UT, but thereafter, it became difficult to distinguish between Aurora 1 and the expanded "Equatorward Aurora" as is shown in the images in Figures 9f and 9g, although Aurora 1 can barely be identified in the image shown in Figure 9g.

Figure 9h shows the temporal variations in the maximum intensities of Aurora 1 and "Equatorward Aurora" together with those of the

Figure 7. The distribution of the latitudinal size of the upward FAC observed by SW-A and SW-C from the two events. The latitudinal size was calculated by multiplying the period of each upward FAC region by satellites' velocity and cos α, where α is an acute angle between the satellite orbit and the MLT meridian.
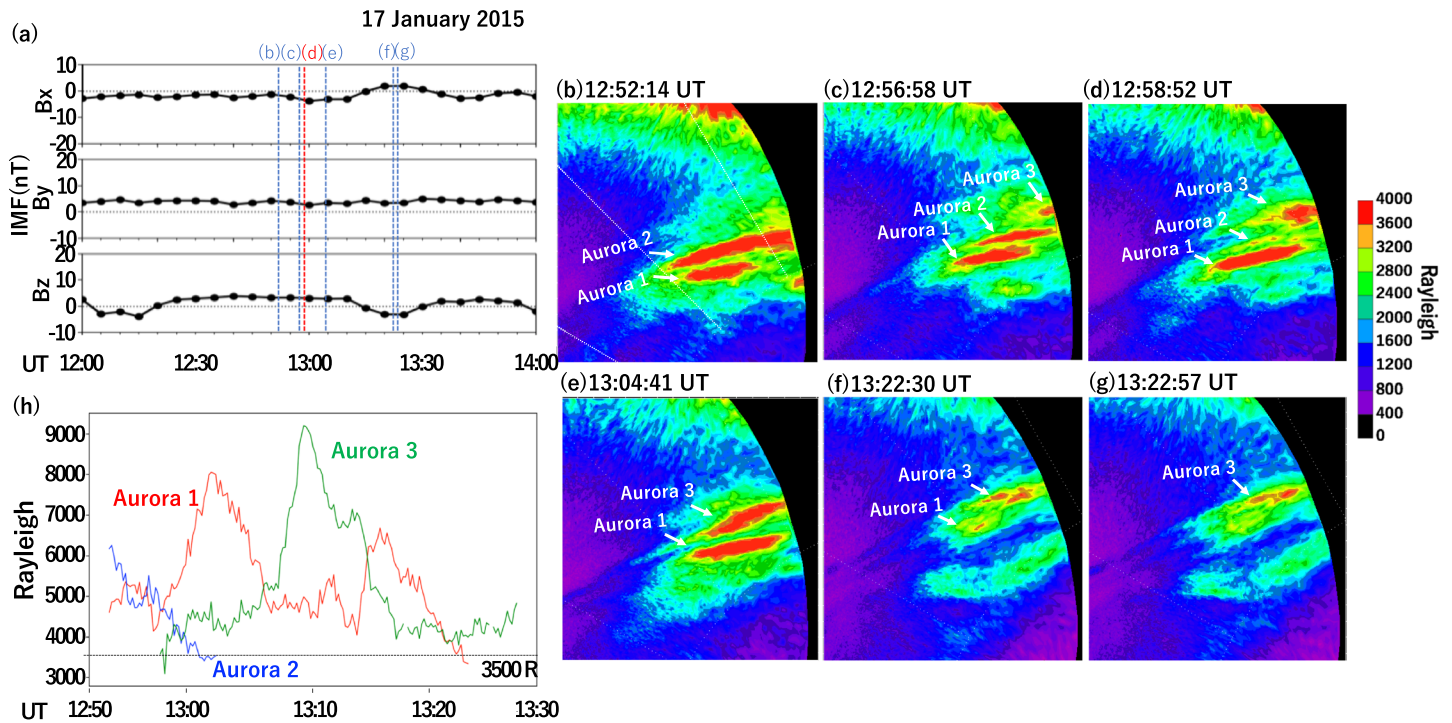
Figure 8. Six aurora images for 17 January 2015 event together with the OMNI IMF data. (a) OMNI IMF B_X, B_Y, and B_Z are plotted from 12:00 to 14:00. The vertical lines b–g represent the time when each aurora image b–g was obtained. (b–g) Six aurora images show the time variations of Auroras 1–3, which are indicated by white arrows. The image d is the same as the one shown in Figure 2i. (h) The time variation of max intensity of three auroras. Each red, blue, and green line indicates Aurora 1, Aurora 2, and Aurora 3, respectively.

polar cap arc. The aforementioned variation for Aurora 1 can be identified in Figure 9h. As was previously noted, the data (red) for Aurora 1 are plotted for the interval after the maximum intensity exceeded 2,500 R (14:08:18 UT) and before ~1530 UT when Aurora 1 was nearly "engulfed" by the equatorward aurora. Aurora 1 was identified for more than 80 min. During the plotted interval, the maximum intensities of the three aurora structures were larger than 3,500 R. If we take this intensity as the threshold for determining the aurora duration, the duration of Aurora 1 is estimated to be approximately 1 hr. From Figure 9h, it is evident that the variations in the three auroral structures are very similar except for during the initial ~20 min, suggesting that the electron precipitations for these three auroral structures are related to a similar magnetospheric condition, which could be achieved during a strongly northward IMF.

4. Discussion

4.1. Source Region of the Mesoscale FAC

Figures 3 and 5 show that 1-Hz magnetic perturbation data obtained by SW-A and SW-C reflect the spatial structure of the mesoscale FACs. Figures 8 and 9 show that enhanced mesoscale auroras continued to exist for at least approximately 30 min, respectively. Coupled with the fact that the mesoscale upward FAC corresponds to the region of the enhanced mesoscale aurora (Figures 3 and 5), it appears that the upward FAC also continued to exist during a similar period of time, suggesting that the FAC has quasipersistent features.

As suggested in Figure 6 (for the 22 December 2014 event), the upward mesoscale FACs flow along the magnetic field lines threading the LLBL. Below this, the upward mesoscale FACs for the 17 January 2015 event are also likely to flow along the magnetic field line threading the LLBL using the Tsyganenko 96 model (Tsyganenko, 1995). The input conditions to the Tsyganenko 96 model are a solar wind dynamic pressure of 1.2 nPa, (IMF B_Y, B_Z) = (3.7, 2.9) nT, and $Dst = -5$ nT.

Figure 10a shows the trajectories of SW-A and SW-C (black lines) on the auroral image obtained at 12:58:52 UT on 17 January 2015. As has been shown in Figure 8d, three auroral structures were observed at this time.
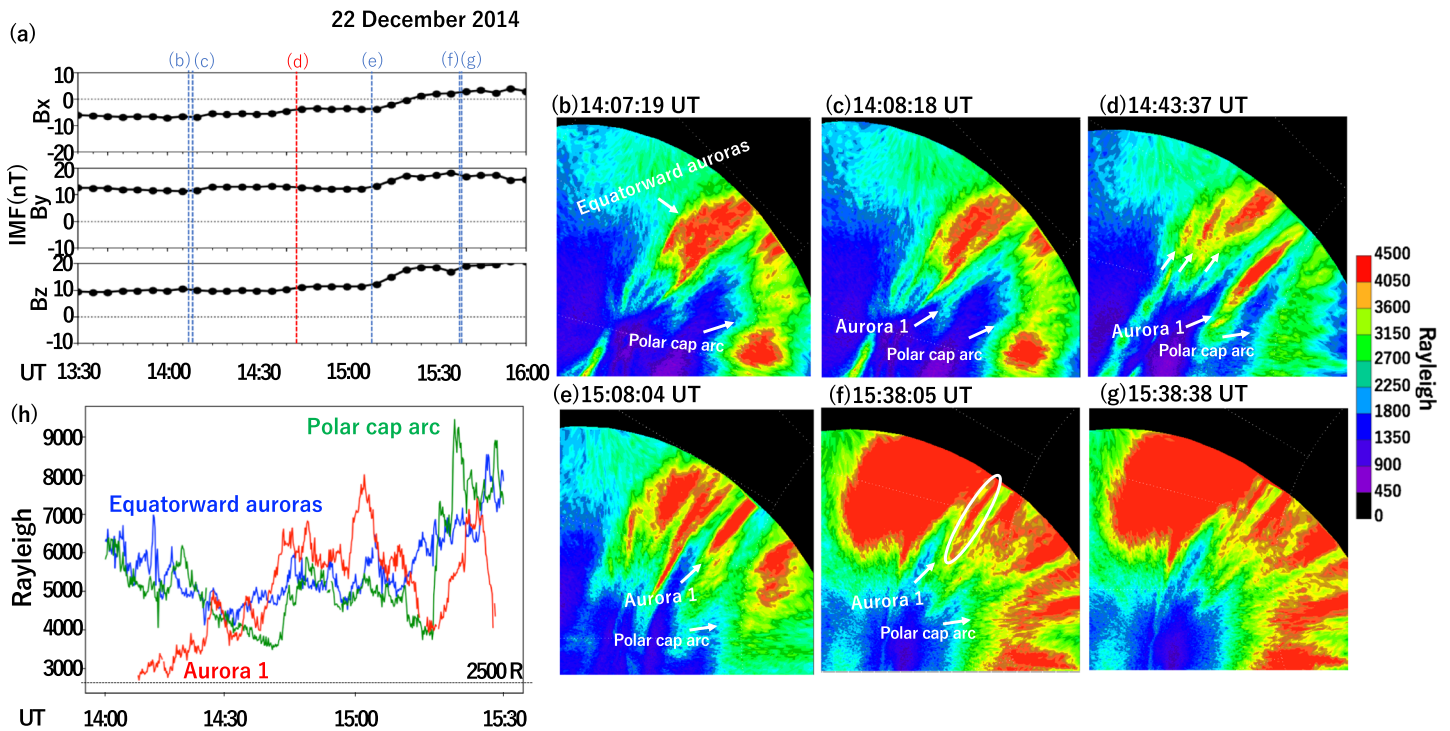
Figure 9. Six aurora images for 22 December 2014 event together with the OMNI IMF data. (a) OMNI IMF B_X, B_Y, and B_Z are plotted from 13:30 to 16:00. The vertical lines b–g represent the time when each aurora image b–g was obtained. (b–g) Six aurora images show the time variations of aurora arcs 1–4, which are indicated by white arrows. Note that there is one more aurora at MLAT > 80°, which is the polar cap arc. The image d is the same as the one shown in Figure 4h, and three adjacent white arrows equatorward of Aurora 1 also correspond to the three adjacent arrows in Figure 4h. (h) The time variation of max intensity of three auroras. Each red, blue, and green line indicates Aurora 1, equatorward auroras, and polar cap arc, respectively. Here, equatorward auroras mean that the chunk of auroras equatorward of Aurora 1, which includes three auroral structures in image d later.

The short thick violet line and blue line, shown as α and β, respectively, indicate the reference lines for the Tsyganenko 96 field line mapping. Each of these lines passes the point of the peak auroral intensity. More specifically, the violet line (Region α) represents the region between (MLAT, MLT) = (78.10, 14.53) and (78.20, 14.53), and the blue line represents the region between (MLAT, MLT) = (78.20,14.67) and (78.70, 14.71). The higher-latitude portions of the trajectory of SW-A (>78.07° MLAT) and that of SW-C (>78.23°) are shown with dotted lines. It is difficult to quantitatively discuss these regions with the field line mapping of the Tsyganenko 96 model because these portions are mapped to a magnetospheric region that is very far from the Earth, that is, downstream of $X_{\mathrm{GSM}} = -60\ R_E$.

Figure 10b shows mapped positions of the Swarm trajectories and Regions α and β with a possible location of the magnetopause. The horizontal axis shows the range between $X_{\mathrm{GSM}} = -30\ R_E$ and $X_{\mathrm{GSM}} = -60\ R_E$, while the vertical axis represents the range between $Y_{\mathrm{GSM}} = 23\ R_E$ and $Y_{\mathrm{GSM}} = 26\ R_E$, that is, the duskside magnetosphere. The solid red line represents the magnetopause location calculated using an empirical magnetopause model by Shue et al. (1998). The two solid black lines, which run nearly parallel to each other, represent the mapped positions of the trajectories of SW-A or SW-C. Notably, these mapped trajectories are within approximately 1 R_E of the empirical duskside magnetopause for $X_{\mathrm{GSM}} = -30\ R_E$ to approximately $-50\ R_E$.

Øieroset et al. (2008) examined magnetosheath plasma penetration for a northward and strongly positive IMF B_Y, which is a similar IMF condition to that of the event of 17 January 2015, and showed that the thickness of the dayside postnoon LLBL is 0.9 R_E. Considering the general tendency for the thickness of the LLBL to increase with increasing distance from the subsolar point (Haerendel et al., 1978), the thickness of the duskside LLBL downstream of $X_{\mathrm{GSM}} = -30\ R_E$ would be greater than 1 R_E for that IMF condition. This suggests that in the present event, SW-A and SW-C passed through the region whose magnetic field lines thread the LLBL. Figure 10b also shows that Regions α and β are mapped to the region immediately (0.1–0.2 R_E)
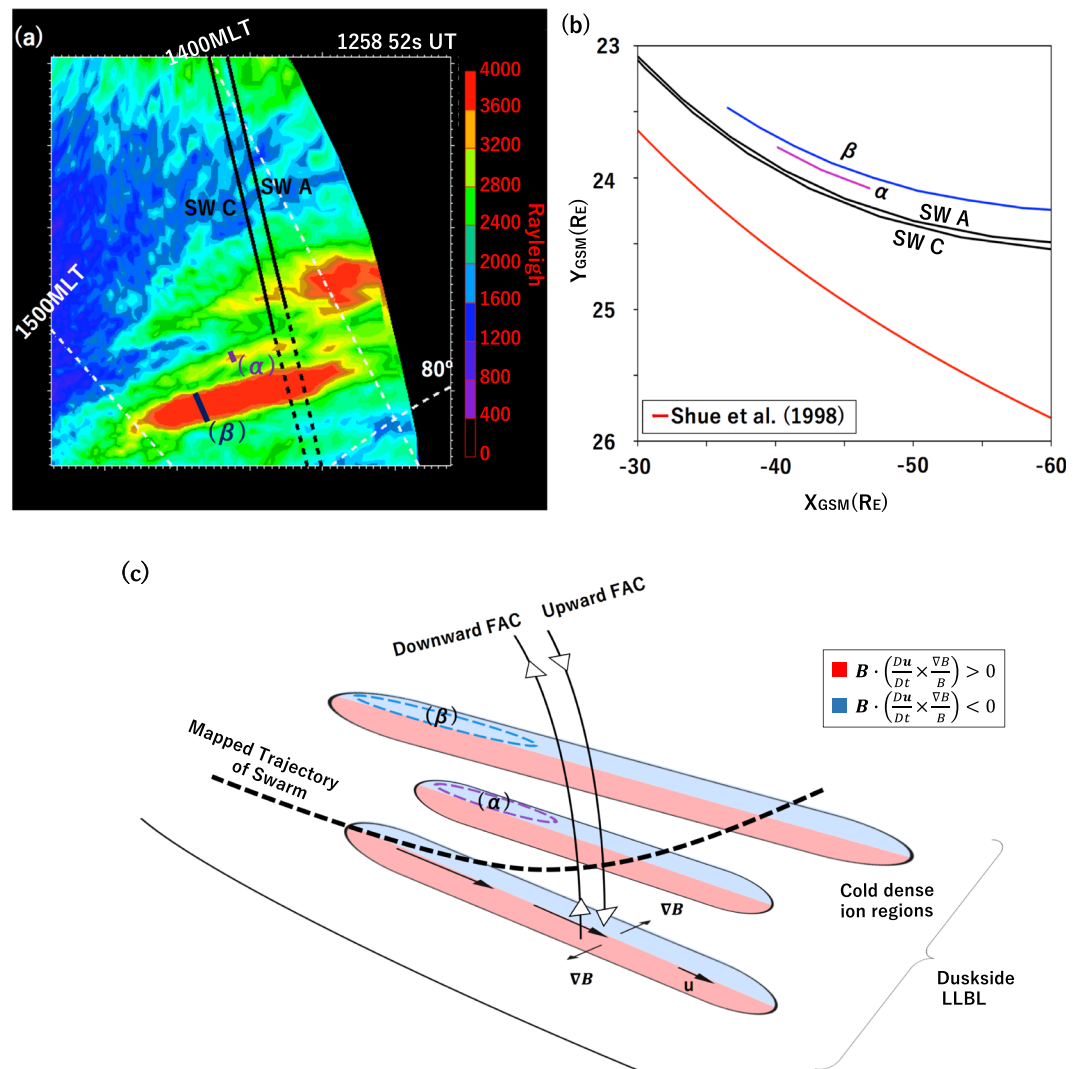
Figure 10. (a) The trajectories of SW-A and SW-C (thin black lines) on the auroral image obtained at 12:58:52 UT on 17 January 2015. (b) The magnetosphere footprints projected along the magnetic field lines using Tsyganenko 96 model. Mapped positions of the Swarm trajectories and Regions α and β (violet and blue thick lines in Figure 10a) are shown with a possible location of the magnetopause calculated with a model by Shue et al. (1998). (c) A possible configuration of the source for the mesoscale FAC coming into the equatorial plane in the duskside LLBL, reflected on the features for the event of 17 January 2015. There are multiple FAC source regions elongating in the X_{GSM} direction. Regions α and β are, respectively, a part of the different FAC source regions. The thick dotted arrow represents the mapped trajectory of Swarm. Red and blue regions indicate the source regions of downward and upward FACs, respectively.

away from the mapped Swarm trajectories. This implies that the magnetic field lines in Regions α and β also thread the LLBL.

Figure 10c shows a possible configuration of the source for the mesoscale FACs in the duskside LLBL. Three pairs of current generation regions are illustrated such that the features for the 17 January 2015 event can be reflected; however, the point is that there are multiple source regions in the dusk LLBL. Our interpretation is that the FACs are generated in the region where the cold dense ions originating from the magnetosheath are significantly decelerated in the LLBL.

When the flow braking occurs in the region where the gradient of the magnetic field exists, a FAC is generated. This can be expressed as follows (e.g., Strangeway, 2012):

$$(\boldsymbol{B} \cdot \nabla)\left(\frac{\boldsymbol{j} \cdot \boldsymbol{B}}{B^2}\right) = \frac{2\boldsymbol{B}}{B^2} \cdot \left(\rho \frac{D\boldsymbol{u}}{Dt} \times \frac{\nabla B}{B}\right), \tag{1}$$

where $\boldsymbol{B}$, $\boldsymbol{j}$, and ρ are the magnetic field, current density, and plasma mass density, respectively. The left-hand part of (1) is the field-aligned gradient of the current density per unit magnetic flux. Its positive (or negative) value represents the FAC flowing away from (or into) the source region in the magnetosphere, that is, a downward (or upward) FAC in the ionosphere. The red and blue parts in Figure 10c illustrate the regions where (1) has positive and negative values, respectively. Assuming that the magnetic field is weakened in the central part of the cold dense plasma because of its high pressure, the gradient of the magnetic field occurs in the outer part of the cold dense plasma region. When the moving cold dense plasma is decelerated, a pair of FACs is generated as is illustrated as the red and blue regions in Figure 10c.

Regions α and β, respectively, represent two separate regions, in which FACs are flowing in. Region β is inside Region α. There is one more region outside Region α. This represents Aurora 3 as shown in Figure 8. The thick dotted line represents the mapped trajectory of SW-A or SW-C. The trajectory is shown in such a manner that it can traverse the three source regions. Considering that the Region 1 FAC between 1400 and 1800 MLT most frequently maps to the boundary plasma sheet (Wing et al., 2010), the mesoscale multiple FACs, whose source region is likely to be in the LLBL, are not simple remnants of the typical Region 1.

4.2. Comparison With Previous Studies on Multiple Discrete Arcs in the Dusk Sector

We have presented events for which the enhanced mesoscale auroras continued to exist in the dusk sector for at least approximately 30 min. In the dusk sector, multiple discrete arcs whose lifetimes are very short, that is, 1–5 min, can also occur. Moen et al. (1994) showed that these arcs lie equatorward of the convection reversal boundary on closed field lines between 1400 and 1500 MLT. Considering the short lifetime, Moen et al. (1994) related them to plasma penetration events from the magnetosheath (Lundin & Evans, 1985) or to kinetic Alfvén wave modes converted from large-scale magnetohydrodynamic surface waves (e.g., Kelvin-Helmholtz waves).

Milan et al. (1999, 2001) showed that highly quasiperiodic poleward moving auroral forms with repetition rates near 1–2 min occurred on field lines just equatorward of the open/closed field line boundary during southward IMF and associated those phenomena with field line resonances (Southwood, 1974). Periodic multiple discrete arcs have also been reported. Mathews et al. (2004) observed periodic multiple discrete arcs propagating sunward and equatorward from the poleward boundary of the auroral oval between 1600 and 1700 MLT. They ascribed these features to periodic Alfvén waves associated with field line resonances.

Zhang et al. (2016) suggest that, under a northward IMF, cusp aligned polar cap arcs occur due to multiple electron precipitation by the velocity shear caused by Kelvin-Helmholtz waves on the low-latitude magnetopause and are produced by Kelvin-Helmholtz and/or interchange instability. In our 22 December 2014 event, multiple polar cap arcs were observed poleward vicinity of the mesoscale FACs and became unable to distinguish them from the auroras caused by the mesoscale FACs afterward.

Recently, Wu et al. (2017) examined multiple arcs associated with multipolar and unipolar FACs by comparing ground-based optical data with magnetic field and electric field data from Swarm satellites. Their "high-quality events" of a multipolar current sheet occur between 19 and 3 MLT (their Figure 3b). This is outside the region of our interest, but the typical arc width associated with the multipolar current sheet is from 10 to 50 km (their Figure 6b), which is consistent with our result of the width of the upward FAC (Figure 7).

5. Conclusions

We examined two events in which the Swarm satellites observed highly structured magnetic perturbations in the 1400–1800 MLT auroral latitudes where large-scale Region 1 and Region 2 are absent. The simultaneous observations from the Swarm satellites and the all-sky imager showed the following features:

1. Very high correlations between SW-A and 9-s shifted SW-C magnetic perturbations demonstrate that these perturbations, which were obtained at 1-Hz resolution, are because of the mesoscale structure of

京都大学
KYOTO UNIVERSITY

A Self-archived copy in
Kyoto University Research Information Repository
https://repository.kulib.kyoto-u.ac.jp

京都大学学術情報リポジトリ
KURENAI 紅
Kyoto University Research Information Repository

the quasistatic FACs, not dynamic Alfvén waves. The typical latitudinal size of the mesoscale upward FACs is 20–30 km.

2. In each region of the mesoscale upward FACs, 630-nm aurora emissions are relatively strong, indicating that the energy flux of electron precipitations having energies of a few hundred electron volts is high in each of the upward FAC regions. The enhanced mesoscale auroras continued to exist over at least approximately 30 min. These findings indicate that the mesoscale FAC structures are also stable during these time periods. In other words, the highly structured FACs have quasipersistent features.

3. The precipitating particle data from the DMSP satellite, which passed through the field of view of the all-sky imager, indicate that the source of the precipitating particles is the duskside LLBL. The Tsyganenko magnetosphere model also suggests that the ionospheric regions of the enhanced auroras are connected to the duskside LLBL.

4. We suggest that the highly structured quasipersistent FACs, which become prominent in the absence of large-scale Region 1/2, flow along the magnetic field lines connected to the duskside LLBL where cold dense ions occur. Considering that the magnetospheric source of the typical Region 1 that can be intensified with the increase in the southward component of the IMF lies in the plasma sheet boundary layer, the highly structured FACs in the duskside auroral oval are phenomena that are pertinent to the magnetosphere for a northward IMF condition, and not a simple remnant of the typical Region 1.

References

Baker, K. B., & Wing, S. (1989). A new magnetic coordinate system for conjugate studies at high latitudes. *Journal of Geophysical Research*, *94*(A7), 9139–9143. https://doi.org/10.1029/JA094iA07p09139

Elphinstone, R. D., Jankowska, K., Murphree, J. S., & Cogger, L. L. (1990). The configuration of the auroral distribution for interplanetary magnetic field B_Z northward: 1. IMF B_X and B_y dependencies as observed by the Viking satellite. *Journal of Geophysical Research*, *95*(A5), 5791–5304. https://doi.org/10.1029/JA095iA05p05805

Friis-Christensen, E., Lühr, H., & Hulot, G. (2006). SW-A constellation to study the Earth's magnetic field. *Earth, Planets and Space*, *58*(4), 351–358. https://doi.org/10.1186/BF03351933

Fujimoto, M., Terasawa, T., Mukai, T., Saito, Y., Yamamoto, T., & Kokubun, S. (1998). Plasma entry from the flanks of the near-Earth magnetotail: Geotail observations. *Journal of Geophysical Research*, *103*(A3), 4391–4408. https://doi.org/10.1029/97JA03340

Gjerloev, J. W., Ohtani, S., Iijima, T., Anderson, B., Slavin, J., & Le, G. (2011). Characteristics of the terrestrial field-aligned current system. *Annales de Geophysique*, *29*(19), 1713–1729. https://doi.org/10.5194/angeo-29-1713-2011

Gussenhoven, M. S. (1982). Extremely high latitude auroras. *Journal of Geophysical Research*, *87*(A4), 2401–2412.

Haerendel, G., Paschmann, G., Sckopke, N., Rosenbauer, H., & Hedgecock, P. C. (1978). The frontside boundary layer of the magnetosphere and the problem of reconnection. *Journal of Geophysical Research*, *83*(A7), 3195–3216. https://doi.org/10.1029/JA083iA07p03195

Hasunuma, T., Nagatsuma, T., Kataoka, R., Takahashi, Y., Fukunishi, H., Matsuoka, A., & Kumamoto, A. (2008). Statistical study of polar distribution of mesoscale field-aligned currents. *Journal of Geophysical Research*, *113*, A12214. https://doi.org/10.1029/2008JA013358

Hosokawa, K., Taguchi, S., Ogawa, Y., & Aoki, T. (2013). Periodicities of polar cap patches. *Journal of Geophysical Research: Space Physics*, *118*, 447–453. https://doi.org/10.1029/2012JA018165

Ishii, M., Sugiura, M., Iyemori, T., & Slavin, J. A. (1992). Correlation between magnetic and electric field perturbations in the field-aligned current regions deduced from DE 2 observations. *Journal of Geophysical Research*, *97*(A9), 13,877–13,887. https://doi.org/10.1029/92JA00110

Iyemori, T. (1988). A statistical study of ULF waves observed by Magsat at ionospheric altitude. *Proceedings of NIPR Symposium Upper Atoms Physics*, *1*, 146–152.

Lühr, H., Park, J., Gjerloev, J. W., Rauberg, J., Michaelis, I., Merayo, J. M. G., & Brauer, P. (2015). Field-aligned currents' scale analysis performed with the Swarm constellation. *Geophysical Research Letters*, *42*, 1–8. https://doi.org/10.1002/2014GL062453

Lundin, R., & Evans, D. S. (1985). Boundary layer plasmas as a source for high-latitude, early afternoon, auroral arcs. *Planetary and Space Science*, *33*(12), 1389–1406. https://doi.org/10.1016/0032-0633(85)90115-1

Mathews, J. T., Mann, I. R., Rae, I. J., & Moen, J. (2004). Multi-instrument observations of ULF wave-driven discrete auroral arcs propagating sunward and equatorward from the poleward boundary of the duskside auroral oval. *Physics of Plasmas*, *11*(4), 1250–1259. https://doi.org/10.1063/1.1647137

Matsuoka, A., Tsuruda, K., Hayakawa, H., Mukai, T., Nishida, A., Okada, T., et al. (1993). Electric field fluctuations and charged particle precipitation in the cusp. *Journal of Geophysical Research*, *98*(A7), 11,225–11,234. https://doi.org/10.1029/92JA01791

Milan, S. E., Sato, N., Miyake, E., & Moen, J. (2001). Aurora forms and the field-aligned current structure associated with filed line resonances. *Journal of Geophysical Research*, *106*, 25,825–25,833. http://doi.org/10.1029/2001JA900077

Milan, S. E., Yeoman, T. K., Lester, M., Moen, J., & Sandholt, P. E. (1999). Post-noon two-minute period pulsating aurora and their relationship to the dayside convection pattern. *Annales Geophysicae*, *17*(877), 1999.

Moen, J., Sandholt, P. E., Lockwood, M., Egeland, A., & Fukui, K. (1994). Multiple, discrete arcs on sunward convecting field lines in the 14–15 MLT region. *Journal of Geophysical Research*, *99*(A4), 6113–6123. https://doi.org/10.1029/93JA03344

Øieroset, M., Phan, T. D., Angelopoulos, V., Eastwood, J. P., McFadden, J., Larson, D., et al. (2008). THEMIS multi-spacecraft observations of magnetosheath plasma penetration deep into the dayside low-latitude magnetosphere for northward and strong B_y IMF. *Geophysical Research Letters*, *35*, L17S11. https://doi.org/10.1029/2008GL033661

Pakhotin, I. P., Mann, I. R., Lysak, R. L., Knudsen, D. J., Gjerloev, J. W., Rae, I. J., et al. (2018). Diagnosing the role of Alfvén waves in magnetosphere-ionosphere coupling: Swarm observations of large amplitude nonstationary magnetic perturbations during an interval of northward IMF. *Journal of Geophysical Research: Space Physics*, *123*, 326–340. https://doi.org/10.1002/2017JA024713

Papitashvili, V. O., & Rich, F. J. (2002). High-latitude ionospheric convection models derived from defense meteorological satellite program ion drift observations and parameterized by the interplanetary magnetic field strength and direction. *Journal of Geophysical Research*, *107*(A8), 1198. https://doi.org/10.1029/2001JA000264

Rich, F. J., & Gussenhoven, M. S. (1987). The absence of Region 1/Region 2 field-aligned current during prolonged quiet times. *Geophysical Research Letters*, *14*(7), 689–692.

Roble, R. G., & Rees, M. H. (1977). Time-dependent studies of the aurora: Effects of particle precipitation on the dynamic morphology of ionospheric and atmospheric properties. *Planetary and Space Science*, *25*(11), 991–1010. https://doi.org/10.1016/0032-0633(77)90146-5

Shue, J.-H., Song, P., Russell, C. T., Steinberg, J. T., Chao, J. K., Zastenker, G., et al. (1998). Magnetopause location under extreme solar wind conditions. *Journal of Geophysical Research*, *103*(A8), 17691–17700. https://doi.org/10.1029/98JA01103

Southwood, D. J. (1974). Some features of field line resonances in the magnetosphere. *Planetary and Space Science*, *22*(3), 483–491. https://doi.org/10.1016/0032-0633(74)90078-6

Strangeway, R. J. (2012). The relationship between magnetospheric processes and auroral field-aligned current morphology. In A. Keiling, E. Donovan, F. Bagenal, & T. Karlsson (Eds.), *Auroral phenomenology and magnetospheric processes: Earth and other planets* (pp. 355–364). Washington, DC: American Geophysical Union. https://doi.org/10.1029/2012GM001211

Taguchi, S., Hosokawa, K., & Ogawa, Y. (2015). Investigating the particle precipitation of a moving cusp aurora using simultaneous observations from the ground and space. *Progress in Earth and Planetary Science*, *2*(1), 1–11. https://doi.org/10.1186/s40645-015-0044-7

Taguchi, S., Hosokawa, K., Ogawa, Y., Aoki, T., & Taguchi, M. (2012). Double bursts inside a poleward-moving auroral form in the cusp. *Journal of Geophysical Research*, *117*, A12301. https://doi.org/10.1029/2012JA018150

Taguchi, S., Sugiura, M., Winningham, J. D., & Slavin, J. A. (1993). Characterization of the IMF B_y-dependent field-aligned currents in the cleft region based on DE 2 observations. *Journal of Geophysical Research*, *98*(A2), 1393–1407. https://doi.org/10.1029/92JA01014

Terasawa, T., Fujimoto, M., Mukai, T., Saito, Y., Yamamoto, T., Machida, S., et al. (1997). Solar wind control of density and temperature in the near-Earth plasma sheet: WIND-GEOTAIL collaboration. *Geophysical Research Letters*, *24*(8), 935–938. https://doi.org/10.1029/96GL04018

Thébault, E., Finlay, C. C., Beggan, C. D., Alken, P., Aubert, J., Barrois, O., et al. (2015). International geomagnetic reference field: The 12th generation. *Earth, Planets and Space*, *67*(1), 79. https://doi.org/10.1186/s40623-015-0028-9

Tsyganenko, N. A. (1995). Modeling the Earth's magnetospheric magnetic field confined within a realistic magnetopause. *Journal of Geophysical Research*, *100*(A4), 5599–5612. https://doi.org/10.1029/94JA03193

Weimer, D. R. (2001). Maps of ionospheric field-aligned currents as a function of the interplanetary magnetic field derived from Dynamics Explorer 2. *Journal of Geophysical Research*, *106*(A7), 12,889–12,902. https://dx.doi.org/10.1029/2000JA000295

Weimer, D. R., Goertz, C. K., Gurnett, D. A., Maynard, N. C., & Burch, J. L. (1985). Auroral zone electric fields from DE 1 and 2 at magnetic conjunctions. *Journal of Geophysical Research*, *90*(A8), 7479–7494. https://doi.org/10.1029/JA090iA08p07479

Wing, S., Ohtani, S., Newell, P. T., Higuchi, T., Ueno, G., & Weygand, J. M. (2010). Dayside field-aligned current source regions. *Journal of Geophysical Research*, *115*, A12215. https://doi.org/10.1029/2010JA015837

Wu, J., Knudsen, D. J., Gillies, D. M., Donovan, E. F., & Burchill, J. K. (2017). Swarm observation of field-aligned currents associated with multiple auroral arc systems. *Journal of Geophysical Research: Space Physics*, *122*, 10,145–10,156. https://doi.org/10.1002/2017JA024439

Zhang, Y., Paxton, L. J., Zhang, Q. -H., & Xing, Z. (2016). Polar cap arcs: Sun-aligned or cusp-aligned? *Journal of Atmospheric and Solar-Terrestrial Physics*, *146*, 123–128. https://doi.org/10.1016/j.jastp.2016.06.001